NAVAL POSTGRADUATE SCHOOL

MONTEREY, CALIFORNIA

THESIS

SIMULATION AND DESIGN METHODS FOR FREE-ELECTRON LASER SYSTEMS

by

Robert A. Neuerman

December 2009

Thesis Advisor:	William B. Colson
Co-Advisor:	Joe Blau

Approved for public release; distribution is unlimited

REPORT DOCUMENTATION PAGE

Form Approved OMB No. 0704-0188

1. AGENCY USE ONLY *(Leave blank)*

2. REPORT DATE December 2009

3. REPORT TYPE AND DATES COVERED Master’s Thesis

4. TITLE AND SUBTITLE Simulation and Design Methods for Free-electron Laser Systems

5. FUNDING NUMBERS

6. AUTHOR(S) Robert A. Neuerman

7. PERFORMING ORGANIZATION NAME(S) AND ADDRESS(ES)
Naval Postgraduate School
Monterey, CA 93943-5000

8. PERFORMING ORGANIZATION REPORT NUMBER

9. SPONSORING /MONITORING AGENCY NAME(S) AND ADDRESS(ES)
N/A

10. SPONSORING/MONITORING AGENCY REPORT NUMBER

11. SUPPLEMENTARY NOTES The views expressed in this thesis are those of the author and do not reflect the official policy or position of the Department of Defense or the U.S. Government.

12a. DISTRIBUTION / AVAILABILITY STATEMENT
Approved for public release; distribution is unlimited

12b. DISTRIBUTION CODE

13. ABSTRACT (maximum 200 words)

Modeling and simulation have proven invaluable to the design of various systems and planning of many experiments since the free-electron laser was invented in the 1970s. This thesis illustrates methods used for these tasks and for the validation and development of further theory. FEL systems and their components are described, briefly discussing how they fit into design considerations. Basic theory of FEL operation is reviewed, including the resonance condition, FEL wave and pendulum equations, and the concepts of undulator taper, extraction and beam quality. Two computer programs used for FEL simulation (*FEL3D*/*FEL4D*, developed at the Naval Postgraduate School, and *Ginger*, developed at Lawrence Berkeley National Laboratory) are discussed and compared, then applied to specific FEL cases. The cases studied serve to evaluate key performance characteristics of FELs. The final case study directly compares output from the two programs. In addition to this type of physics simulation, computer tools are also vital for component design. Relevant methods are illustrated using the example of an electrostatic cathode test cell and drawings made using the Los Alamos National Laboratories design tool, *Poisson Superfish*. After reviewing the principles involved and system constraints, a new test cell is designed for use with future NPS experiments. The effects of anode-cathode spacing and anode aperture size are examined for two different anode configurations and recommendations are made for future design iterations.

14. SUBJECT TERMS Free-electron lasers, FEL simulations, undulators, FEL oscillators, FEL amplifiers, diamond field-emitter arrays, field emission cathodes, cathode test cell

15. NUMBER OF PAGES 65

16. PRICE CODE

17. SECURITY CLASSIFICATION OF REPORT	**18. SECURITY CLASSIFICATION OF THIS PAGE**	**19. SECURITY CLASSIFICATION OF ABSTRACT**	**20. LIMITATION OF ABSTRACT**
Unclassified	Unclassified	Unclassified	UU

NSN 7540-01-280-5500

Standard Form 298 (Rev. 2-89)
Prescribed by ANSI Std. 239-18

THIS PAGE INTENTIONALLY LEFT BLANK

SIMULATION AND DESIGN METHODS FOR FREE-ELECTRON LASER SYSTEMS

Robert A. Neuerman
Lieutenant, United States Navy
B.S., Rensselaer Polytechnic Institute, 2004

Submitted in partial fulfillment of the
requirements for the degree of

MASTER OF SCIENCE IN APPLIED PHYSICS

from the

NAVAL POSTGRADUATE SCHOOL
December 2009

Author: Robert A. Neuerman

Approved by: William B. Colson
Thesis Advisor

Joseph Blau
Co-Advisor

Andrès Larraza
Chairman, Department of Physics

ABSTRACT

Modeling and simulation have proven invaluable to the design of various systems and planning of many experiments since the free-electron laser was invented in the 1970s. This thesis illustrates methods used for these tasks and for the validation and development of further theory. FEL systems and their components are described, briefly discussing how they fit into design considerations. Basic theory of FEL operation is reviewed, including the resonance condition, FEL wave and pendulum equations, and the concepts of undulator taper, extraction and beam quality. Two computer programs used for FEL simulation (*FEL3D*/*FEL4D*, developed at the Naval Postgraduate School, and *Ginger*, developed at Lawrence Berkeley National Laboratory) are discussed and compared, then applied to specific FEL cases. The cases studied serve to evaluate key performance characteristics of FELs. The final case study directly compares output from the two programs.

In addition to this type of physics simulation, computer tools are also vital for component design. Relevant methods are illustrated using the example of an electrostatic cathode test cell and drawings made using the Los Alamos National Laboratories design tool, *Poisson Superfish*. After reviewing the principles involved and system constraints, a new test cell is designed for use with future NPS experiments. The effects of anode-cathode spacing and anode aperture size are examined for two different anode configurations and recommendations are made for future design iterations.

THIS PAGE INTENTIONALLY LEFT BLANK

TABLE OF CONTENTS

THIS PAGE INTENTIONALLY LEFT BLANK

LIST OF FIGURES

LIST OF TABLES

THIS PAGE INTENTIONALLY LEFT BLANK

LIST OF ACRONYMS AND ABBREVIATIONS

APPLE	Advanced Planar Polarized Light Emitter
DC	Direct-current
DFEA	Diamond Field-emitter Array
ERL	Energy-recovery Linac
FE	Field Emission
FEL	Free-electron Laser
JLab	Thomas Jefferson National Laboratory
LANL	Los Alamos National Laboratory
LBNL	Lawrence Berkeley National Laboratory
LINAC	Linear Accelerator
LLNL	Lawrence Livermore National Laboratory
NPS	Naval Postgraduate School
RF	Radio-frequency
RMS	Root-mean-square
SASE	Self-amplifying Stimulated Emission

THIS PAGE INTENTIONALLY LEFT BLANK

ACKNOWLEDGMENTS

I would like to extend special thanks to Dr. William Fawley of Lawrence Berkeley National Laboratory for allowing the use of *Ginger* for this thesis, and for his generous help and guidance to a new user.

THIS PAGE INTENTIONALLY LEFT BLANK

I. INTRODUCTION

Free-electron lasers (FELs) are, like any other lasers, sources of coherent electromagnetic radiation (light), which is amplified by stimulated emission from electrons. Free-electron lasers differ from other types, however, in how the light is generated. Rather than relying on electrons bound within matter, FELs use a high-energy beam of electrons in vacuum. They are distinguished from solid-state and gas lasers by the flexibility of their designs: Adjustment of a few system parameters completely alters their output wavelength, whereas conventional lasers are restricted by the quantum properties of their lasing media. Some of the relevant FEL parameters will be set during system construction; but others, such as the electron beam energy, can be altered continuously, allowing wide flexibility in application.

Years of study with FELs have also shown the systems to be powerful, reliable (98% or more uptime on many systems) and efficient (10%–20% wall-plug efficiency according to some estimates). On the other hand, FEL systems have historically been large and expensive; a smaller footprint and the ability to be supported on mobile platforms are active areas of research for some applications.

Modeling and simulation have proven invaluable to the design of various systems and planning of many experiments since the free-electron laser was invented in the 1970s. This thesis illustrates methods used for these tasks and for the validation and development of further theory.

Chapter II describes FEL systems and their components, briefly discussing how they fit into design considerations. Chapter III reviews the basic theory of FEL operation, including the resonance condition, FEL wave and pendulum equations, and the concepts of undulator taper, extraction and beam quality. Chapter IV discusses and compares two computer programs used for FEL simulation (*FEL3D*/*FEL4D*, developed at the Naval Postgraduate School, and *Ginger*, developed at Lawrence Berkeley National Laboratory) and applies them to study specific FEL cases. The cases studied serve to familiarize readers with the simulations' output and highlight key performance characteristics of FELs. The final case study directly compares output from the two programs.

Chapter V delves into the specifics of physical design, using the example of an electrostatic cathode test cell and drawings made using the Los Alamos National Laboratories design tool, *Poisson Superfish*. The principles and design constraints for a test cell to be used with future NPS experiments are examined. The effects of anode-cathode spacing and anode aperture size are studied for two different anode configurations and recommendations are made for future design iterations.

II. FREE-ELECTRON LASER SYSTEM DESCRIPTION

Free-electron lasers can have two basic configurations: oscillator or amplifier. Most components are common to both designs, as shown in Figure 1. The difference is how the light is extracted from the electron beam—amplifiers amplify an existing optical field over one pass while oscillators use optical resonators similar to conventional lasers. The following sections discuss the purpose and general properties of the system components. Figure 1 depicts a particular FEL system with a few illustrative properties:

1. Separate beam paths for running in oscillator or amplifier mode. This shows the difference between the two, but the dual beamline configuration can be found in real systems, such as the experimental setup at Thomas Jefferson National Laboratory.

2. A superconducting radio-frequency linear accelerator, and the helium refrigeration plant associated with it. Normal-conducting systems are also used widely. Electrostatic (DC) and storage ring accelerators have also been used for FELs.

3. Beam recirculation for energy recovery (see "Beam Disposal" below).

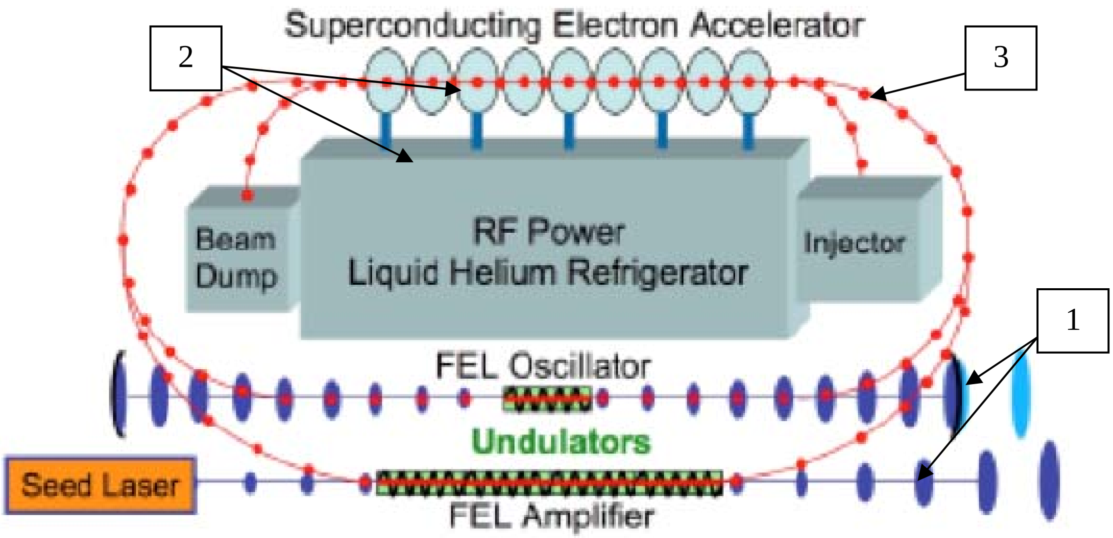

Figure 1. FEL System Schematic

A. INJECTOR

The injector generates the beam of free electrons from a cathode. Cathodes come in several varieties and generally produce electrons either via thermionic emission, the photoelectric effect or field emission. Thermionic cathodes emit electrons when electrically heated to a point where the thermal energy in the metal exceeds its work function. Photocathodes emit electrons due to the photoelectric effect. When they are illuminated by a drive laser, as long as the energy per photon exceeds the work function, electrons are liberated. Field-emission cathodes are not necessarily metal, and use geometry to create points where high electric fields exist once an external potential is applied. For example, diamond field-emitter array (DFEA) cathodes are wafers of diamond film grown on a suitable substrate such that the diamond forms an array of microscopic pyramids; the field is enhanced enough at the pyramids' tips that electrons escape by Folwer-Nordheim tunneling.

Regardless of cathode type, injectors will apply some external field to the emitted electrons, accelerating them to modest energies before they enter the accelerator component. There will also be some amount of instrumentation and beam transport apparatus (e.g., focusing magnets) to prepare the beam for entry to the accelerator and to perform initial characterization of the electron beam.

Injector design can be important to overall system performance in that it must provide electrons to the accelerator with optimal bunch length and repetition frequency. Furthermore, the beam quality (i.e., the spatial or angular spread of the electrons or the relative disparity of their kinetic energies; see discussion in Chapter III) provided by the injector is the highest that will be present in the entire system.

B. ACCELERATOR

The electron beam is next passed through an accelerator, which raises its energy to the desired level. Direct-current (DC) acceleration is possible, but high-energy applications usually use radio-frequency (RF) fields. Electron accelerators generally consist of a series of evacuated metal cavities to which external RF power is applied in order to generate strong electromagnetic fields inside. The alternating fields can be timed so as to provide net positive acceleration to the sequence of electron pulses provided by the injector.

C. UNDULATOR

The undulator consists of a series of alternating transverse magnetic fields, which produce transverse accelerations of the electron beam. This causes the electrons to radiate, producing spontaneous emission like population inversion does in a conventional laser. The transverse motion of the electrons also allows for transfer of energy between the electrons and the optical field, stimulating further emission, creating a coherent light source. The relativistic speeds of the electrons ensure this optical field takes the form of a narrow coaxial beam.

Undulators can be linear or helical in their polarization. Linear undulators (see Figure 2) consist of a series of dipole magnets, alternating in orientation, which create a magnetic a field that is periodic in one transverse plane.

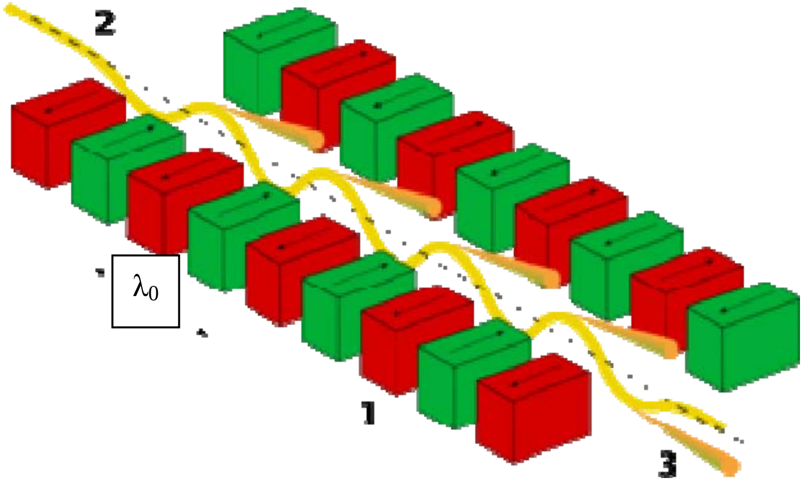

Figure 2. Linear Undulator, showing (1) Magnets, (2) Electron Beam and (3) Synchrotron Radiation (not discussed) [After 1]

Helical undulators, as shown in Figure 3, usually consist of permanent magnets or electromagnets coiled around the beam path in a helix, and provide a magnetic field that is periodic in both transverse directions (see Chapter III). There are also planar-geometry undulators that can provide a helical magnetic field, such as the APPLE (Advanced

Planar Polarized Light Emitter) system [2]. In the APPLE, two linear undulators are operated with their planes of polarization at an angle to one another, thus producing net polarization that can be helical (elliptical or circular) or linear in a specified direction, depending to the angle used.

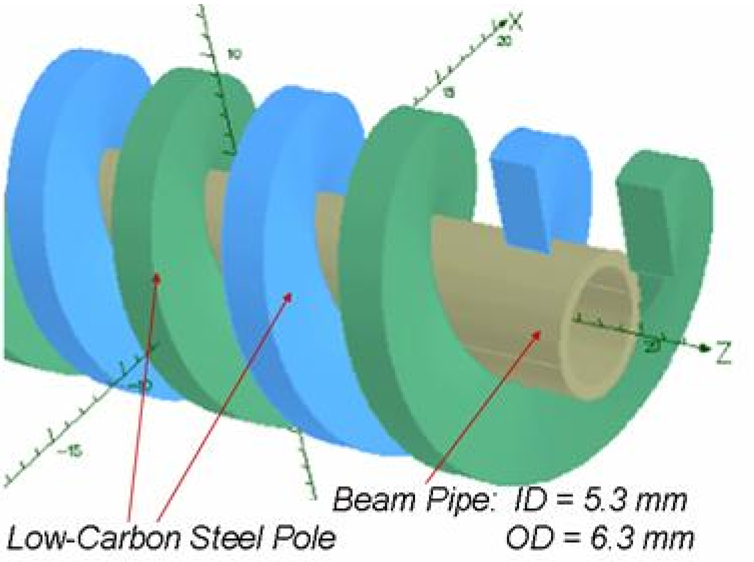

Figure 3. Helical Undulator [From 3]

D. OPTICAL COMPONENTS

In FEL oscillator designs, the undulator is contained in a resonator cavity, with one fully reflective and one partially transmissive mirror. As the light repeatedly transits this resonator, it serves to stimulate further emission from new electrons. On each pass, a portion of the light is outcoupled via the partially transmissive mirror. In most FEL amplifier designs, the initial optical field is produced by a seed laser that is amplified while passing only once through the undulator. There are also self-amplifying stimulated-emission (SASE) designs that use the spontaneously-emitted light from the first portion of the undulator as a seed. Amplifier designs, in general, require longer undulators than oscillators, with SASEs requiring significantly more length.

E. BEAM TRANSPORT AND DIAGNOSTICS

The physical layout of the FEL system will determine exactly which components, such as bending magnets and focusing magnets, are required to properly transport the beam. Most systems will also have several types of diagnostics at various places along the beamline, both for application-specific purposes and to track the results of beam transport.

F. BEAM DISPOSAL

After light is generated in the undulator, one must dispose of the spent electrons. Ultimately, the beam's energy can be dissipated into something as simple as a metal target as long as appropriate cooling and radiation shielding are provided. This is labeled as "Beam Dump" in Figure 1. Since light generation only depletes a small fraction of the electrons beam's energy, some designs recirculate the beam through the accelerator; if re-injected with the proper phase, the electrons will give up significant energy to the RF fields, boosting system efficiency and making beam disposal much less hazardous. This technique is referred to as "energy recovery," and linear accelerators that use it (not all of which are FELs) are known as "energy-recovery linacs" or ERLs.

THIS PAGE INTENTIONALLY LEFT BLANK

III. BASIC FREE ELECTRON LASER THEORY

The centerpiece of FEL physics is the interaction between electrons and light that takes place within the undulator. The physics of particle acceleration and laser beam transport are vital to the operation of the greater system; but the undulator is where the interaction characteristics of free-electron lasers are determined.

It is helpful to begin a mathematical description of these interactions by defining a few useful coordinates:

$$\begin{aligned} &\tau \equiv \frac{ct}{L} \\ &\zeta \equiv (k+k_0)z-\omega t, \text{ and} \\ &\nu \equiv \frac{d\zeta}{d\tau} = L[(k+k_0)\beta_z - k]. \end{aligned} \qquad \{3.1\}$$

The normalized time τ serves as a temporal variable along the longitudinal spatial coordinate; $\tau = 0$ corresponds to the beginning of the undulator and $\tau = 1$ to its end. The electron phase ζ measures an electron's relative position in a portion of the electron beam the length of one optical wavelength λ, and the electron phase velocity ν measures its rate of change. Here z is the electron's position along the undulator; $\omega = kc$ is the frequency of the optical field; L is the length of the undulator; $k = 2\pi/\lambda$ and $k_0 = 2\pi/\lambda_0$ are the wave numbers corresponding to the optical wavelength λ and undulator period λ_0 respectively; and $\beta_z = v_z/c$ is the normalized longitudinal electron velocity. We will see that these definitions play an important role in the free-electron laser's interaction.

A. RESONANCE CONDITION AND PENDULUM EQUATION

The electrons' motion is determined by the Lorentz force equations, namely

$$\begin{aligned} &\frac{d(\gamma\vec{\beta})}{dt} = -\frac{e}{mc}\left(\vec{E}+\vec{\beta}\times\vec{B}\right), \text{ and} \\ &\frac{d\gamma}{dt} = -\frac{e}{mc}\vec{\beta}\cdot\vec{E}. \end{aligned} \qquad \{3.2\}$$

For a helical undulator (see Chapter II), the magnetic field can be expressed as

$$\vec{B}_{und} = B(\cos[k_0 z], \sin[k_0 z], 0), \qquad \{3.3\}$$

while the optical fields will take the form

$$\begin{aligned} \vec{E} &= E(\cos\psi, -\sin\psi, 0) \\ \vec{B}_{opt} &= E(\sin\psi, \cos\psi, 0), \text{ where} \\ \psi &\equiv kz - \omega t + \varphi. \end{aligned} \qquad \{3.4\}$$

In the preceding equations, E is the optical electric field strength, B is the undulator's magnetic field strength, φ is the field phase, and e and m are the charge magnitude and mass of an electron. In Equation {3.2}, the pertinent magnetic field is the sum $\vec{B} = \vec{B}_{und} + \vec{B}_{opt}$.

Substituting {3.3} and {3.4} into {3.2} and assuming that $\beta_{\mathrm{z}} \approx 1$ gives the transverse motion as

$$\begin{aligned} \vec{\beta}_{\perp} &= -\frac{K}{\gamma}(\cos[k_0 z], \sin[k_0 z], 0), \text{ where} \\ K &\equiv \frac{eB_{rms}\lambda_0}{2\pi mc^2}. \end{aligned} \qquad \{3.5\}$$

The "undulator parameter" K is a dimensionless measure of field strength and is of order unity. Note that this derivation assumes ideal injection into a helical undulator such that, when solving for position as a function of time, the constants of integration are all zero. In the helical case, $B_{\mathrm{rms}} = B$; but a similar analysis holds for linear undulator geometry with $B_{\mathrm{rms}} = B/\sqrt{2}$.

The evolution of electron energy can be analyzed through changes in γ and in v. In particular, from the second equation in {3.2} and Equation {3.5}:

$$\frac{d\gamma}{dt} = \frac{eKE}{\gamma mc}\cos(\zeta + \varphi). \qquad \{3.6\}$$

The electron's velocity is related to its energy and hence its Lorentz factor γ, specifically,

$$\gamma^{-2} = 1 - \beta_{\perp}^2 - \beta_z^2. \qquad \{3.7\}$$

Equation {3.5} shows that the magnitude of the transverse velocity is merely K / γ; thus, for $\gamma \gg 1$, Equation {3.7} reduces to

$$\beta_z = \sqrt{1 - \frac{1+K^2}{\gamma^2}} \approx 1 - \frac{1+K^2}{2\gamma^2}. \qquad \{3.8\}$$

As an aside, we consider next the condition under which optimum energy transfer occurs between the electron beam and optical field—referred to as "resonance." In this state, each electron emits (or amplifies) one wavelength's worth of light (λ) for each undulator period (distance λ_0) through which it passes. If the interaction between the electron and the optical field is thought of as a race down the undulator, then the light leads in velocity by $c(1-\beta_z)$ and wins by a distance of λ in one undulator period. The time passed is

$$\Delta t = \frac{\lambda_0}{c\beta_z}. \qquad \{3.9\}$$

The winning distance can be expressed as the velocity difference multiplied by the race time:

$$\lambda = c(1-\beta_z)\Delta t = \lambda_0 \frac{1-\beta_z}{\beta_z}. \qquad \{3.10\}$$

From Equation {3.8}, we see that the condition for resonance is

$$\begin{aligned} &\frac{\lambda}{\lambda_0} = \left(\frac{1}{\beta_z} - 1\right), \text{ or, for } \gamma \gg 1, \\ &\lambda \approx \lambda_0 \frac{1+K^2}{2\gamma^2}, \end{aligned} \qquad \{3.11\}$$

which relates the FEL's output wavelength to fundamental properties of the electron beam and undulator. This important relation highlights the tunable and designable nature of FELs. Adjustment of any or all of the system parameters that impact K allows designers to build systems that emit at any of a wide range of wavelengths, or even to adjust K on an existing system.

Using the "resonance condition," Equation {3.11}, in the definition of phase velocity, and recognizing that $k \gg k_0$ (i.e., $\gamma \gg 1$) shows that

$$\nu = \frac{d\zeta}{d\tau} = L\left[(k+k_0)\left(1-\frac{1+K^2}{2\gamma^2}\right)-k\right] \approx -Lk\left(\frac{1+K^2}{2\gamma^2}\right), \text{ and}$$
$$d\nu \approx \frac{2\pi L}{\lambda}\left(-\frac{1+K^2}{2\gamma^2}\right)(-2)\frac{d\gamma}{\gamma} = \left(\frac{4\pi L}{\lambda_0}\right)\frac{d\gamma}{\gamma}. \qquad \{3.12\}$$

From the definition of undulator period ($L = N\ \lambda_0$, where N is the number of periods), we find

$$d\nu = 4\pi N\frac{d\gamma}{\gamma}. \qquad \{3.13\}$$

Differentiating ν with respect to τ and using the result of Equation {3.6} gives:

$$\frac{d\nu}{d\tau} = \frac{d^2\zeta}{d\tau^2} = |a|\cos(\zeta+\varphi), \text{ where}$$
$$|a| \equiv \frac{4\pi NeKLE}{\gamma^2 mc^2}. \qquad \{3.14\}$$

This is known as the “FEL pendulum equation” for its similarities to the equation of motion for a simple pendulum. Using this equation, the evolution of FEL electrons is often described with phase space (ζ vs. ν) graphs.

Parameter a is a dimensionless measure of the laser field amplitude E. Values of $a < \pi$ are considered the “weak field” regime, while $a \gg \pi$ is considered “strong fields.” The FEL theory as presented is valid for both regimes, as well as intermediate values.

B. FEL WAVE EQUATION

The FEL’s optical field will evolve according to Maxwell’s wave equation:

$$\left(\nabla^2 - \frac{1}{c^2}\frac{\partial^2}{\partial t^2}\right)\vec{A}(\vec{x},t) = -\frac{4\pi}{c}\vec{J}(\vec{x},t). \qquad \{3.15\}$$

In this equation, $\vec{A}$ is the optical vector potential and $\vec{J}$ is the transverse current density due to the undulations of the electrons. The vector potential is related to the optical fields by:

$$\vec{E} = -\frac{1}{c}\frac{\partial\vec{A}}{\partial t}, \quad \vec{B} = \nabla\times\vec{A}. \qquad \{3.16\}$$

Assuming a complex optical electric field in the form

$$E(\vec{x},t)=\left|E(\vec{x},t)\right|e^{i\varphi(\vec{x},t)}e^{i\alpha}, \qquad \{3.17\}$$

where $\alpha \equiv kz-\omega t$ represents the carrier wave, the vector potential becomes

$$\vec{A}(\vec{x},t)=\frac{E(\vec{x},t)}{k}\hat{n}e^{i\alpha}, \qquad \{3.18\}$$

where $\hat{n}$ is the polarization vector. Given that the light spectrum produced is not only finite but narrow (i.e., a laser), it is safe to assume that the amplitude and phase vary only slowly along the scale of an optical wavelength ($\lambda = 2\pi / k$) and the scale of the optical frequency ($\omega = kc$). In this case, one can assert

$$\frac{\partial\left|E\right|}{\partial t}\ll\omega\left|E\right|,\quad \frac{\partial\varphi}{\partial t}\ll\omega\varphi,\quad \frac{\partial\left|E\right|}{\partial z}\ll k\left|E\right|,\quad \frac{\partial\varphi}{\partial z}\ll k\varphi. \qquad \{3.19\}$$

Substituting Equation {3.18} into Equation {3.15} and using conditions {3.19} to neglect terms with two derivatives, the relation simplifies to

$$\left[\nabla_{\perp}^{2}+2ik\left(\frac{\partial}{\partial z}+\frac{1}{c}\frac{\partial}{\partial t}\right)\right]E(\vec{x},t)=-\frac{4\pi k}{c}\left(\vec{J}\cdot\hat{n}^{*}\right)e^{-i\alpha}, \qquad \{3.20\}$$

where the transverse Laplacian symbol ($\nabla_{\perp}^{2}$) denotes differentiation only in the *x* and *y* coordinates. In this new parabolic form of the wave equation, the source term can be expressed as

$$\vec{J}(\vec{x},t)=-ec\sum_{i}\beta_{\perp}\delta^{(3)}\left[\vec{x}-\vec{r}_{i}(t)\right]. \qquad \{3.21\}$$

In this expression, $r_{\mathrm{i}}\left(\mathrm{t}\right)$ is the position of the *i*th electron at time *t* and $\vec{\beta}_{\perp}$ is the transverse velocity discussed in Equation {3.5}. For a helical undulator producing circularly polarized light, $\hat{n}=(-i,1,0)$, thus

$$\vec{\beta}_{\perp}=\operatorname{Re}\left(-\frac{K}{\gamma}i\hat{n}e^{-ik_{0}z}\right). \qquad \{3.22\}$$

Invoking the method of characteristics to introduce the coordinate $u \equiv z-ct$ (which follows the light through the evolution), the derivatives in Equation {3.20} are transformed as follows:

$$\begin{aligned}\frac{\partial}{\partial z} &= \frac{\partial}{\partial u}\\ \frac{\partial}{\partial t} &= -c\frac{\partial}{\partial u}+\frac{\partial}{\partial t}.\end{aligned} \qquad \{3.23\}$$

Recalling τ as defined in Equation {3.1}, Equation {3.23} becomes

$$\left[\nabla_{\perp}^{2}+\frac{2ik}{L}\frac{\partial}{\partial\tau}\right]E(\vec{x},t)=-4\pi ieKk\left\langle\frac{e^{-i\zeta}}{\gamma}\right\rangle\rho(\vec{x},t), \qquad \{3.24\}$$

where the notation <*expression*> indicates an average of the expression over all electrons and the electron particle beam density in a small volume element *dV* is

$$\rho(\vec{x},t)=\int_{V}\sum_{i}\delta^{(3)}\left[\vec{x}-\vec{r}_{i}(t)\right]dV. \qquad \{3.25\}$$

To simplify presentation (and mathematics), we utilize the definition of dimensionless laser field amplitude from Equation {3.14} and introduce the dimensionless current density

$$j\equiv\frac{8N\rho(\pi eKL)^{2}}{\gamma^{3}mc^{2}}. \qquad \{3.26\}$$

Values of $j<\pi$ are "low gain" cases, while $j\gg\pi$ is the "high gain" regime; as with the values of *a*, this FEL theory is valid for all values of *j*.

Transforming transverse coordinates to dimensionless form by $\tilde{x}=x\sqrt{k/(2L)}$ and $\tilde{y}=y\sqrt{k/(2L)}$, the final form of the FEL wave equation is obtained:

$$\left(-\frac{i}{4}\tilde{\nabla}_{\perp}^{2}+\frac{\partial}{\partial\tau}\right)a(\vec{x},t)=-\left\langle je^{-i\zeta}\right\rangle. \qquad \{3.27\}$$

The modified Laplacian symbol $\tilde{\nabla}_{\perp}^{2}$ is used here to denote differentiation with respect to the normalized coordinates $\tilde{x}$ and $\tilde{y}$. The terms of Equation {3.27} involving this spatial derivative describe the evolution of the optical field due to diffraction effects. Terms involving the time derivative describe its evolution due to gain from the electron beam. The term $<je^{-i\zeta}>$ is a measure of how strongly bunched the electrons are, showing that this portion of the dynamics have a significant effect on optical output. It is worth noting also that in Equation {3.27}, the evolution of *a* depends on electron distribution ζ, while in {3.14} the evolution of ζ depends on |*a*|; thus, the FEL wave and pendulum equations form a feedback loop. Bunched electrons amplify light better, while the optical field's coherent evolution promotes electron bunching. The gain from this process only grows for so long, however, as electrons will eventually overbunch, at which point the FEL reaches saturation.

C. UNDULATOR TAPER

In high-gain FELs, saturation can be reached before the end of the undulator, lowering overall FEL extraction (see below). This can be overcome by altering the resonance condition, Equation {3.11}, along the length of the undulator. While it is possible to do this by changing the undulator period λ_0, it is more common to alter *K*. This typically involves changing the gap between undulator poles in order to change the magnetic field *B*, so the process is usually referred to as "tapering" the undulator. The effect is to add an additional phase acceleration term to the pendulum equation, giving

$$\begin{aligned} &\frac{d^2\zeta}{d\tau^2} = \delta + \left|a\right|\cos(\zeta + \varphi), \text{ where} \\ &\delta \equiv -4\pi \mathrm{N}\frac{K^2}{1+K^2}\left(\frac{\Delta K}{K}\right). \end{aligned} \qquad \{3.28\}$$

The quantity δ is referred to as the taper rate[4]. For taper rates that are too large ($\delta > \left|a\right|$), the electrons are accelerated away from resonance before they are able to bunch, limiting energy transfer. Rates that are too low ($\delta \leq 4\sqrt{\left|a\right|}$) will provide only a weak effect, and do not enhance the FEL's natural extraction. Since oscillators typically have undulators too short to face this problem, tapering is much more commonly applied to FEL amplifiers[5].

D. EXTRACTION

Up to this point, references to "efficiency" have applied to the overall system. To examine specifically the efficiency of the energy exchange between the electron beam and optical field, one may define the "extraction" as the relative amount of energy transferred from the electron beam to the optical field on a single pass, that is,

$$\eta \equiv \frac{E_{opt}}{E_b} = \frac{\langle \Delta E \rangle}{E_b} = \frac{\langle \Delta \gamma \rangle}{\gamma}, \qquad \{3.29\}$$

where E_{opt} is the energy in the optical field, E_b is that in the electron beam, and $\Delta E = \Delta\gamma mc^2$ is the change in the electron beam energy over the length of the undulator. Since the theoretical FEL gain curve has a width of $\Delta\nu = 2\pi$, it follows from Equation {3.13} that

$$\eta_{\max} = \frac{\langle \Delta \gamma \rangle}{\gamma} = \frac{\langle \Delta \nu \rangle}{4\pi N} \approx \frac{1}{2N}. \qquad \{3.30\}$$

Equation {3.30}, however, applies only to untapered undulators. Introducing taper changes the expression to [5]

$$\eta_{\delta} = \frac{|\delta|}{8\pi N}. \qquad \{3.31\}$$

E. BEAM QUALITY

The derivations of the FEL pendulum Equation, {3.14}, and the FEL wave Equation, {3.27}, assumed that the optical fields were plane waves of infinite transverse extent. This assumption remains valid mathematically so long as the electron beam remains close enough to the center of the optical field and diffraction is small. This places a condition both on the beam's radius and on the angular spread of the electrons. Neither well-collimated beams of large radius nor highly divergent beams of small initial radius will satisfy the assumptions of Parts A and B. One appropriate measure of beam quality, then, is the transverse emittance, defined as

$$\varepsilon \equiv r_b \theta_b, \qquad \{3.32\}$$

where r_b is the root-mean-square (rms) radius of the electron beam and θ_b is its rms angular spread, as illustrated in Figure 4.

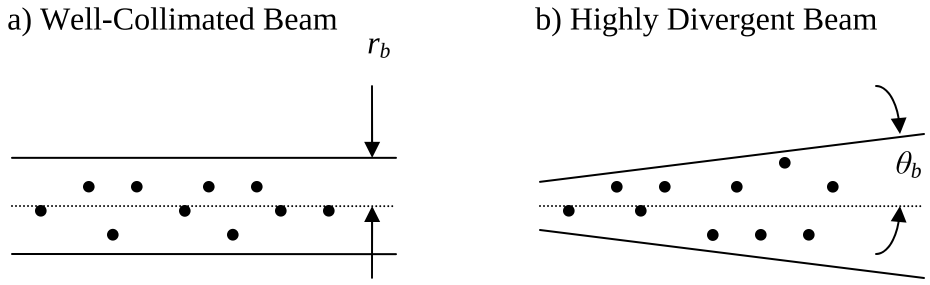

Figure 4. Beam Quality Dimensions

An alternate measure, which has the advantage of being conserved as the beam is accelerated, is the normalized transverse emittance, defined as

$$\varepsilon_n \equiv \gamma r_b \theta_b . \qquad \{3.33\}$$

Equation {3.13} shows that changes in the phase velocity are proportional to the relative change in Lorentz factor, $d\gamma/\gamma$. This is nonzero for a relativistic beam from a particle accelerator because the electrons do not all have the same kinetic energy, and is referred to as the “energy spread.” It is another important measure of the beam’s quality, and it influences the FEL interaction, as well as the beam transport devices (e.g., focusing and defocusing elements).

THIS PAGE INTENTIONALLY LEFT BLANK

IV. SIMULATION MODELS

A. *FEL3D/FEL4D*

Faculty and students at the Naval Postgraduate School have been engaged in theoretical research and numerical modeling of FELs for over twenty years. Their efforts have supported the FEL research community's full spectrum of activity—from design support for new experiments to refining the understanding of experimental results. Over time, the Naval Postgraduate School (NPS) has developed a suite of simulations for both amplifiers and oscillators that have been benchmarked against both theoretical formulas and experimental results. The suite includes four types of programs: single-mode, longitudinal multimode, transverse multimode and four-dimensional [5].

The single-mode simulations follow the phase-space evolution of many electrons and one optical mode (an infinite plane wave) along the undulator, using the pendulum and wave Equations ({3.14} and {3.27}) to self-consistently determine the behavior of both the electrons and the light. They can be used to independently model certain physical effects, allowing for general understanding of the origins and consequences of those effects. They are small and computationally inexpensive, easy to understand, and provide a solid foundation from which to build more comprehensive simulations.

The longitudinal multimode simulations are used to examine the evolution of longitudinal modes in the optical field. The optical amplitude and phase are allowed to vary as a function of z in each longitudinal "slice" of the optical field. Longitudinal modes play an important role in some FELs due to the phenomenon of "pulse slippage." When the pulses are short, the difference in velocities between electron and optical pulses can significantly affect the manner in which the light is amplified.

The transverse multimode simulations, collectively referred to as *FEL3D*, break from the assumption that the optical fields are plane waves. They use the pendulum and wave equations to self-consistently follow the evolution of the electron beam and the optical field in x, y, and τ. They also allow for axial asymmetries, such as separate emittances in the two transverse planes, astigmatism in oscillator mirrors, and shifts or tilts of either the electron beam or the oscillator mirrors. These effects can also have a significant impact on FEL gain and extraction. Both the transverse and longitudinal multimode programs require only moderate computing resources, and run on personal computers, though their efficiency is increased when multiple processors are available.

To provide a more realistic simulation by following both longitudinal and transverse effects, NPS has recently developed the *FEL4D* programs. These model the electrons and the light in *x*, *y*, and *z* while allowing them to evolve in time. These simulations require significant processing time and large amounts of memory, and are used with the dedicated resources of a cluster computer.

B. *GINGER*

The history of the code *Ginger* began with the code *Fred*, a two-dimensional FEL amplifier simulation code developed at Lawrence Livermore National Laboratory (LLNL) some three decades ago. The early spinoffs from *Fred* included a harmonic simulation called *Nutmeg* and a three-dimensional (i.e., multimode) program dubbed *Fred3D*.

Researchers at LLNL and Lawrence Berkeley National Laboratory (LBNL) created *Ginger* in the mid-1980s primarily to examine the physics and consequences of sideband growth in single-pass FEL amplifiers [6]. *Ginger* is polychromatic, time-dependent and multidimensional. It has grown over the years to include many optional features, such as a shot-noise startup model, configurations for complicated FEL types (e.g., harmonic cascade FELs), and higher-harmonic emission models. Historically, it has been limited to axisymmetric (*r*, *z*, *t*) geometry for fields, but recent modifications include optional “slab” geometry (*y*, *z*, *t*, infinite *x*). The simulation can also still be run in a non-time-dependent (3D) configuration, referred to as “*Fred* mode.”

Ginger and its postprocessor are both flexible and powerful. Both are written in *Fortran90* and originally designed for use with *Unix*, but have been successfully ported to various platforms. The simulations explored for this thesis operate efficiently on a desktop computer; larger and more complicated problems can take advantage of the multiprocessor version of the program for use on cluster computers.

C. *FEL3D* CASE STUDY: BEAM QUALITY IN A GENERIC FEL OSCILLATOR

Table 1 represents a parameter set for a generic FEL oscillator. These values do not correspond to any given machine, but are generally illustrative of realistic values and, thus, useful as a case with which to explore a simulation code's operation.

Electron Beam Parameters	
Energy:	$E_b = 120$ MeV
Radius:	$r_b = 0.1$ mm
Bunch charge:	$q = 1$ nC
Bunch duration:	$t_b = 2$ ps
Trans. emittance:	$\varepsilon_n = 10$ mm-mrad
Long. emittance:	$\varepsilon_l = 200$ keV-ps
Peak current:	$I_{peak} = 500$ A
Energy Spread:	$\Delta\gamma/\gamma = 0.2\%$
Undulator Parameters	
Period:	$\lambda_0 = 3$ cm
Length:	$L = 0.75$ m
Gap	$g = 1$cm
Number of periods:	$N = 25$
Undulator parameter:	$K_{\mathrm{rms}} = 1.78$
Resonator Parameters	
Wavelength:	$\lambda = 1.12$ μm
Length:	$S = 20$ m
Rayleigh length:	$Z_0 = 7.5$ cm
Quality factor:	$Q_n = 4$

Table 1. Generic FEL Oscillator Parameters

Most of these quantities are self-explanatory or have been discussed before. Longitudinal emittance is an electron beam quality measure that is proportional to energy spread. The undulator gap g is the spacing between magnet poles, determining the magnetic field strength and, thus, the undulator parameter K. The Rayleigh length Z_0 is the distance from the optical beam waist over which the light will propagate before its cross-sectional area doubles. The optical wavelength value shown is the resonant wavelength of the FEL, determined from beam energy and undulator parameters by Equation {3.11} (recall that $E_b = \gamma mc^2$). The quality factor Q_n represents the losses per pass in the optical resonator, with low Q_n values corresponding to high losses. In a conventional laser, this includes in-cavity losses such as heating in the lasing medium.

For an FEL oscillator, it is used to indicate the amount of power outcoupled through the resonator’s partially transmissive mirror. Ideally, it is related to the outcoupling mirror’s reflectivity *R* by

$$R = 1 - \frac{1}{Q_n} \qquad \{4.1\}$$

The output of *FEL3D* is mostly graphical, though specific numeric quantities can be extracted with simple *Unix* commands. Figure 5 is part of the output for the case outlined in Table 1, depicting the $\tilde{x} = 0$ slice of the optical field after 300 passes. The optical field amplitude $a(0, \tilde{y}, \tau)$ is shown, with lighter blue meaning more intensity. The thin cyan lines correspond to the e^{-1} points relative to the peak amplitude. Spaced along the τ axis are sample electrons (red dots)—the fact that they all fall within the inner portion of the optical field indicates that the beam and field were well-matched. Also depicted at $\tau = 0$ and $\tau = 1$ are line-plots of the optical mode shape, with magenta corresponding to the cavity fundamental mode for reference and yellow to the mode observed in the simulation. Some deviation between the two is typical, especially at $\tau = 1$, and the “hollow” (depressed-peak) mode shown here is not uncommon.

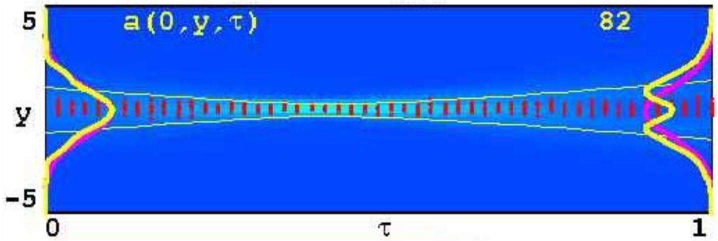

Figure 5. Generic Oscillator: Centerline Optical Field and Electron Beam (*FEL3D*)

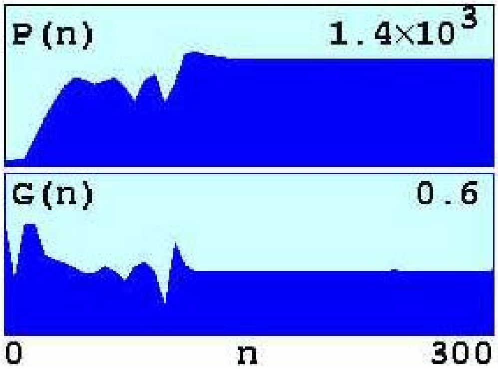

Figure 6. Generic Ocillator: Power and Gain Evolution (*FEL3D*)

Another portion of the output is displayed in Figure 6. This depicts the evolution of outcoupled optical power and optical gain over 300 passes, in normalized units. Both quantities exhibit transient fluctuations for the first 100 or so passes, then reach steady-state.

Several other figures are produced for a given case in *FEL3D* and can be reviewed either to check simulation viability or to look for particular behaviors. Often, however, the goal of a specific design (i.e., parameter set) is a particular quantity, usually the output power or extraction. To demonstrate the *FEL3D* code and gain a general insight into the behavior of FEL oscillators, we conducted a parameter study to determine the extraction against simultaneous variation of transverse emittance and energy spread. All other parameters used the values in Table 1.

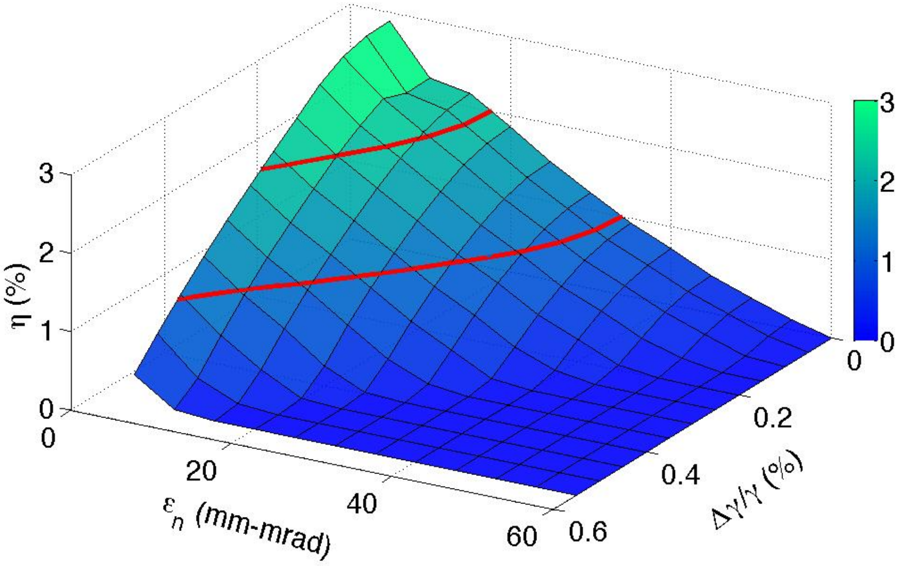

Figure 7. Generic Oscillator: Beam Quality Parameter Study (*FEL3D*)

The results of this study are shown in Figure 7. The results point to the general conclusion that increasing either emittance or energy spread reduces extraction. This is somewhat intuitive, but studies such as these can quantify the dependence. For these parameters, the peak extraction is approximately 3%, a strong but plausible value. The two red contours on this graph correspond to 2% and 1% extraction. Staying above half the peak extraction requires simultaneously keeping the emittance under 30mm-mrad and the energy spread under 0.4%. Both requirements are reasonable values by current standards.

D. *GINGER* CASE STUDY: JLAB'S 14KW EXPERIMENT

In October 2006, Thomas Jefferson National Laboratory (JLab) broke their record for FEL average output power by achieving 14.2kW in continuous-wave oscillator operation. The parameters for that experiment are summarized in Table 2.

Electron Beam Parameters	
Energy:	E_b = 150 MeV
Radius:	r_b = 0.17 mm
Bunch charge:	q = 114 pC
Bunch duration:	t_b =0.4 ps
Peak current:	I_{peak} = 285 A
Avg current:	I_{ave} = 8.5mA
Trans. emittance:	ε_n = 8 mm-mrad
Long. emittance:	ε_l = 80 keV-ps
Energy Spread:	$\Delta\gamma/\gamma$ =0.2%
Undulator Parameters	
Period:	λ_0 = 5.5 cm
Length:	L = 1.65 m
Number of periods:	N = 30
Undulator parameter:	K_{rms} = 1.36
Resonator Parameters	
Length:	S = 32 m
Wavelength:	λ = 1.6 μm
Rayleigh length:	Z_0 = 75 cm
Waist radius:	w_0 = 0.6 mm
Mode radius at mirrors:	w = 1.3 cm
Quality factor:	Q_n = 5

Table 2. JLab 14kW Parameters

These parameters were used to build familiarity with *Ginger* just as the generic FEL oscillator parameters were used to build familiarity with *FEL3D*. A brief comparison shows that the numbers in Tables 1 and 2 are of similar magnitude. More importantly, Table 2 represents a known experiment with known results, which furthermore has been previously simulated by NPS.

The output of *Ginger*'s dedicated postprocessor is a series of graphs. Most of them track different quantities than the output of *FEL3D*, reflecting the difference in the programs' origins. Gain and power evolution, however, are important to any FEL and appear in both codes' output. For the case outlined in Table 2, the gain evolution is shown in Figure 8.

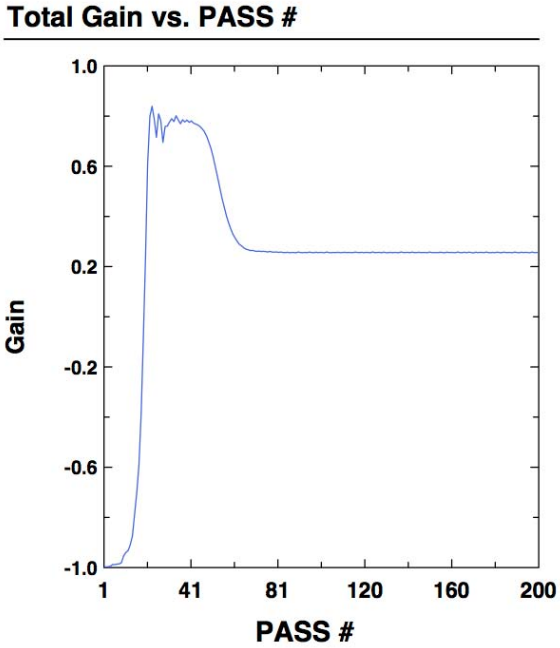

Figure 8. JLab 14kW: Gain Evolution (*Ginger*)

As with the previous example, the simulation shows significant transients over the first one-third of the evolution, then settles into steady-state. The steady-state gain value appears to be approximately 25%. The gain per pass G required for steady-state operation is given by

$$G = \frac{1}{Q_n - 1}, \tag{4.2}$$

or 25% for $Q_n = 5$. This is a simple check that the simulation is behaving as expected and increases confidence in its results.

The power evolution is depicted in Figure 9. The transients are minimal—a simple ramp-up—and the FEL reaches steady-state around pass 60, just as the gain did. This is another check on behavior meeting expectations. The values depicted on this graph are of peak power at the exit of the undulator ($\hat{P}_{und}$). To convert to average outcoupled power ($\overline{P}_{out}$), one must know the pulse duration t_b, the pulse repetition frequency Ω and quality factor Q_n. The formula relating them is

$$\overline{P}_{out} = \hat{P}_{und}\left(\frac{t_b\Omega}{Q_n}\right). \qquad \{4.3\}$$

For this experiment, the quality factor and pulse duration are given in Table 2, while the PRF is approximately 75MHz. Using 1.7GW for $\hat{P}_{und}$ yields $\overline{P}_{out} \approx 10.2\text{kW}$.

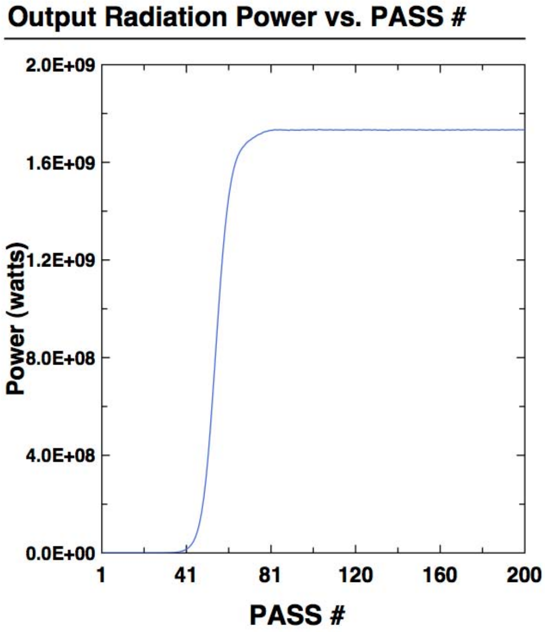

Figure 9. JLab 14kW: Power Evolution (*Ginger*)

While this result is approximately 27% below the known experimental results, it is of the correct order of magnitude. Furthermore, previously conducted NPS 3D simulations predicted nearly 20kW, a 40% overestimation. The conclusion drawn at the time was that pulse slippage effects were present in the experiment, which would reduce the predicted output power.

E. COMPARATIVE CASE STUDY: BEAM QUALITY IN A GENERIC FEL AMPLIFIER

To compare the results of *FEL3D* and *Ginger*, we took the case of a generic FEL amplifier, using the parameters in Table 3. The values chosen match closely with the generic FEL oscillator parameters from Part C by design. The most notable difference is the significant increase in undulator length, typical for amplifier designs. Additionally, the optical cavity parameters have been replaced by seed laser specifications. The seed wavelength, which will also be the output wavelength, is determined entirely by the type of seed laser used and therefore typically driven by the needs of the application. In this case, the value was chosen to match the output wavelength of the generic oscillator.

Electron Beam Parameters	
Energy:	E_b =120 MeV
Radius:	r_b =0.3 mm
Bunch charge:	q =1 nC
Bunch Duration:	t_b =2 ps
Trans. Emit:	ε_n = 10 mm-mrad
Long. emit:	ε_l = 200 keV-ps
Peak Current:	I_{peak} = 500 A
Energy Spread:	$\Delta\gamma/\gamma$ =0.2%
Undulator Parameters	
Period:	λ_0 = 3 cm
Length:	L = 3.6 m
Gap	1 cm
Number of periods:	N = 120
Undulator parameter:	K_{rms} = 1.78
Seed Laser Parameters	
Wavelength:	λ = 1.12 μm
Pulse Duration:	t_{opt} = 4 ps
Average power:	P_{opt} = 1 W
Peak power:	P_{peak} = 330 kW

Table 3. Generic FEL Amplifier Parameters

Using *FEL3D*, we conducted a parameter study on beam quality. As before, we varied transverse emittance and energy spread simultaneously and noted output extraction. For this version of the study, we included a taper rate of $\Delta B / B = 5\%$ over the last meter of the undulator. The results are shown in Figure 10.

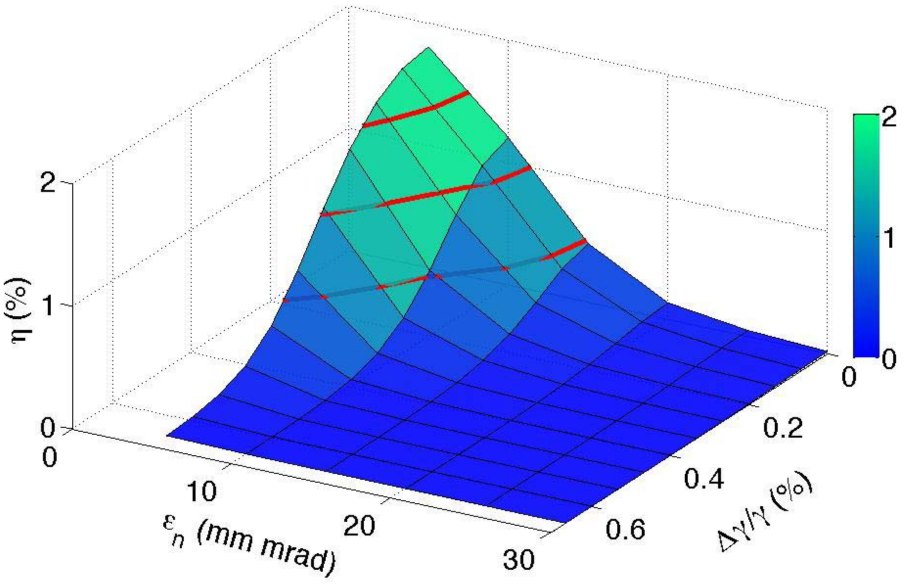

Figure 10. Generic Amplifier: Beam Quality Parameter Study (*FEL3D*)

Peak extraction for this case was somewhat lower than for the oscillator, near two percent. This is a normal and desirable value by current design standards. To stay above half this peak value, it was observed that the design must maintain transverse emittance below 10mm-mrad and energy spread below 0.25%. Recall that the corresponding limits for the oscillator were 30mm-mrad and 0.4%. This amplifier, then, is shown to be more sensitive to beam quality than a similar oscillator. This result is consistent with known experiments and the underlying physics. Put simply, amplifiers have significantly longer undulators; therefore, any degradation the beam quality introduces to the interaction is compounded over a longer time and has a greater effect. In an oscillator, each pass an optical pulse makes through the resonator is a new interaction with new electrons, so beam quality effects are essentially “reset” each time.

For the code comparison, we examined the variation of emittance and energy spread separately. Figure 11 shows the results of varying emittance while holding energy spread constant at 0.2%.

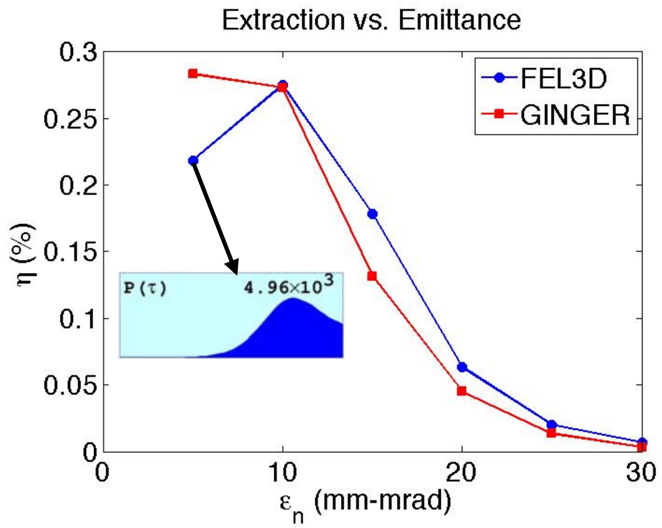

Figure 11. Generic Amplifier: Extraction vs. Emittance (Comparative)

The agreement between the codes is close. The only notable discrepancy occurs for the minimum emittance value. Neither simulation included taper in this case; the inset figure displays the power evolution from *FEL3D*, which shows clearly that the interaction reached saturation before the end of the undulator.

Figure 12 shows the results of varying energy spread while holding emittance at 10mm-mrad. Again, the codes agree very well until low values of energy spread. The inset indicates the same reasons as above for this discrepancy.

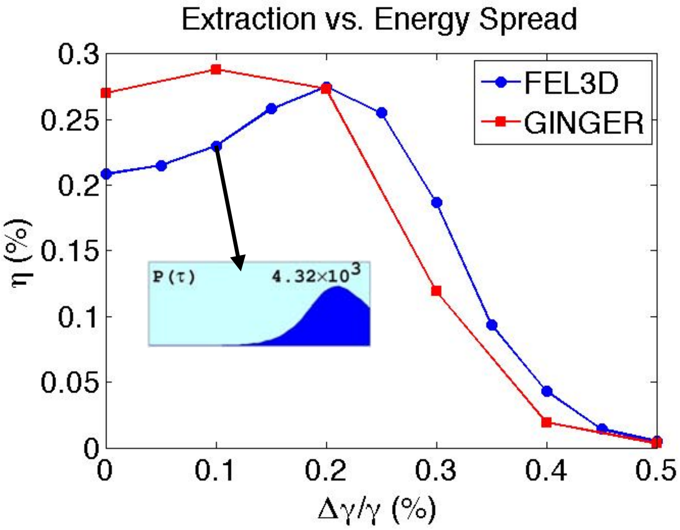

Figure 12. Generic Amplifier: Extraction vs. Energy Spread (Comparative)

F. CONCLUSIONS

The two simulation codes considered—*FEL3D* and *Ginger* in its 3D mode—appear consistent. Some variation in the detailed results should be expected due to internal differences in the simulations. The strongest disparity seen in our examination came from the Jefferson Lab 14kW results, which *Ginger* underestimated and *FEL3D* overestimated. Both results, however, were of the correct order, and both discrepancies are likely due to the lack of pulse-slippage effects in the models. In direct comparison, the two codes agreed very well on beam-quality effects in a generic FEL amplifier. The discrepancies seen here show that the NPS models reached saturation early and therefore exhibited a lower extraction than they would have with a taper.

V. ELECTROSTATIC CATHODE TEST CELL DESIGN

As discussed in Chapter II, design of an injector is important to overall design of a free electron laser (FEL). Characterization of the cathode used is important to the design of any injector. Normally, since injectors are generally not built to support more than one cathode type, this is performed on a “one-off” basis for the cathodes used by a given FEL. Additionally, replacing a cathode is often an involved task, undertaken only when the one in use has been spent or damaged.

A tool the FEL community finds useful is the cathode test cell: a device that is not a full-fledged injector but can be used to test and characterize different cathodes under quasi-operational conditions. Due to the significant differences between the physical nature of and measurements required for thermionic, photoelectric, and field emission cathodes, the test cell design presented in this thesis focuses only on one type, namely field emission (FE). Existing FE test cells include the one used to explore diamond field-emitter array (DFEA) cathodes at Vanderbilt University (Figure 13). Typically, test cells achieve high fields with low voltages using small anode-cathode spacing (“gap”). At higher voltages, the small gap and gridded anode can result in subjecting the device and the cathode to significant damage from vacuum arcing and ion blowback.

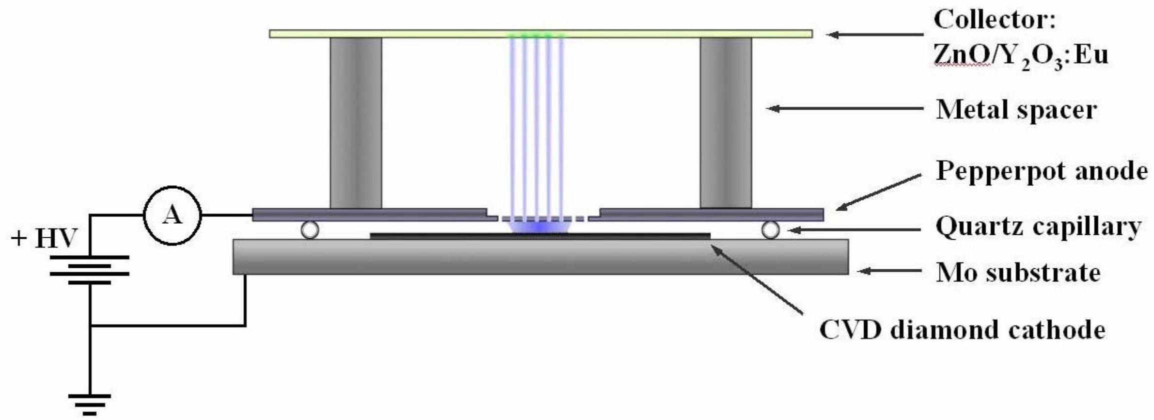

Figure 13. Vanderbilt’s DFEA Test Stand [From 7]

The general goal for the design presented in this chapter is for a higher-voltage, larger-gap, non-gridded test cell. Building such a device will allow NPS researchers to explore the properties of FE cathodes at higher voltages and gain general experience with FE cathodes for possible use in their future FEL experimental facility. The design work discussed here presents preliminary considerations—building a foundation upon which future research will build, until a final design is selected and the system procured.

A. FIELD EMISSION THEORY

Cold (i.e., not thermionic) field electron emission can occur at the surface of a bulk material when strong static external electric fields are applied. It arises from the phenomenon of quantum tunneling and its explanation in the 1920s was one of the early triumphs in the then-emerging field of quantum mechanics. (It is also important due to its many practical applications, included devices such as the test cell under discussion.) The current density J emitted in the presence of applied field E is given by the Fowler-Nordheim equation, a simplified form of which is [8]

$$J = AE^2 e^{-B/E}. \qquad \{5.1\}$$

The constants A (in units of A/V^2) and B (in units of V/m) are related to the material's work function φ and Fermi energy ε_f by

$$\begin{aligned} A &= \frac{6.2\cdot 10^{-3}}{\varphi+\varepsilon_f}\sqrt{\frac{\varepsilon_f}{\varphi}} \\ B &= (6.8\cdot 10^{9})\varphi^{3/2} \end{aligned} \qquad \{5.2\}$$

Several other, more complicated, forms of the Fowler-Nordheim equation exist, since several methods have been used to derive the fundamental form of the coefficients A and B. Equation {5.1} is presented in this form to illustrate the most salient points of the formula: inverse exponential dependence on E and variation with material properties. The fundamental principle is that a larger field will yield more current.

When the surface of the bulk material is not perfectly planar, any protrusions will cause local field enhancements (field lines will converge at their tips), effectively multiplying the applied field by a geometry-dependent factor at those points. This significantly lowers the overall field E required to reach a given value of current density

J. The field *E* as used in Equation {5.1} remains the pertinent value at the tips. This occurs naturally due to the microprotrusions (i.e., surface roughness) of bulk materials, but it can also be deliberately exploited by building in macroscopic protrusions.

Diamond field emitter arrays (see Figure 14) take advantage of this technique. A thin layer of diamond is grown on a wafer of a suitable substrate such that the diamond forms into an array of pyramids. When placed in an external field, the pyramids serve as field-enhancement points and can emit electrons, which will be accelerated by the applied field and form beamlets. Arrays can be fairly dense (in terms of tips per unit area) to provide high current density, but this will cause space-charge forces to affect the beamlets' propagation.

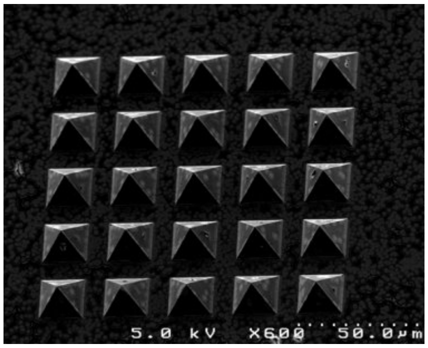

Figure 14. Example of a DFEA [After 9]

B. TEST CELL DESIGN REQUIREMENTS

A cathode test cell must apply a given field to the cathode being tested and allows characterization or monitoring of the cathode's performance. Proper characterization of an FE cathode involves measuring the current emitted as a function of field and time, and monitoring the beam shape, which will have an effect on beam transport and emittance. For DFEA cathodes, this is sometimes analyzed on a per-tip basis; for sparse enough arrays, the beam from each separate tip can be monitored. To support testing of multiple cathodes, the cathode holder should be easily removable. To facilitate varying the field strength *E*, either the power supply voltage *V* must be variable, or the cathode assembly should be movable, allowing for adjustment of the anode-cathode gap *d*, or both. For the ideal case—where the anode and cathode are infinite parallel plates—the three quantities are related by

$$E = V / d. \qquad \{5.3\}$$

Operation of a field-emission (FE) cathode requires a vacuum chamber—any gas present would be ionized by the electron beam and likely damage the cathode. Figure 15 displays the insulating ceramic upon which this test cell design was based. Its metal flanges are separated by a ceramic break, allowing the components at either end to be electrically isolated from one another. The flanges are of a standard type ("conflat"), compatible with many common devices and fittings. Custom fittings can easily be ordered once the required configuration of measurement devices, power ports, vacuum system ports, etc., are fully determined.

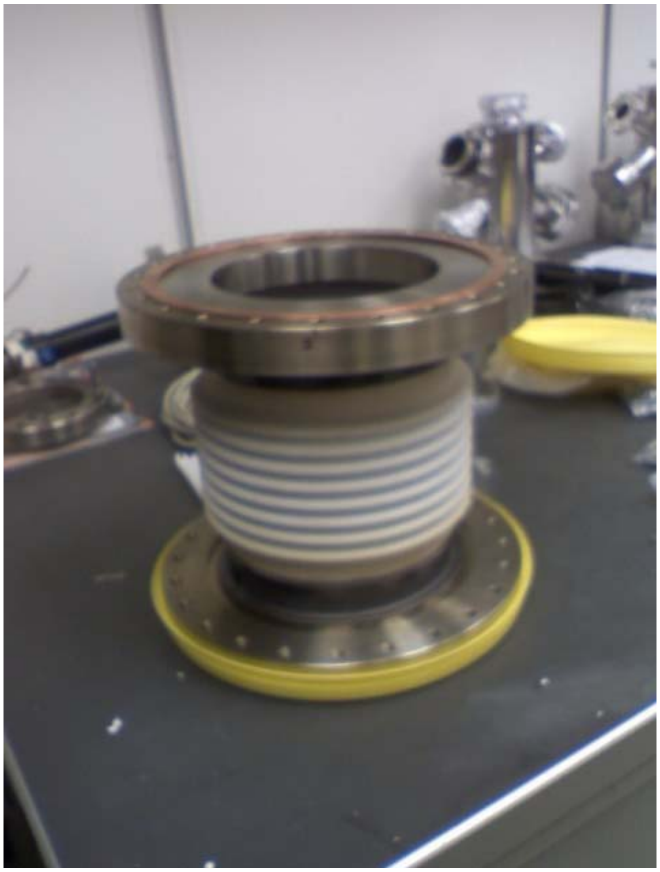

Figure 15. Ceramic Insulator with Conflat Flanges

The electron beam's size can be analyzed by placing a phosphor screen in the beam's path and observing the spot(s) illuminated upon it. The phosphor screen can also serve as a charge collector, with current easily measured across a resistor placed between it and ground. The stability of the current measured can be monitored using a current transformer placed around any isolated portion of the chamber through which the beam travels. Using the type of cylinder depicted in Figure 15, one can conceive of an arrangement such as shown in Figure 16.

Here, the movable cathode assembly is fixed to an endcap that is bolted to the lower flange, allowing for easy removal. This end is held at a large negative voltage during operation. The annular anode is electrically coupled to the other endcap, which contains the phosphor screen (beam target) and is grounded during operation. Figure 16 provides the basis for the preliminary test cell design presented in the following sections.

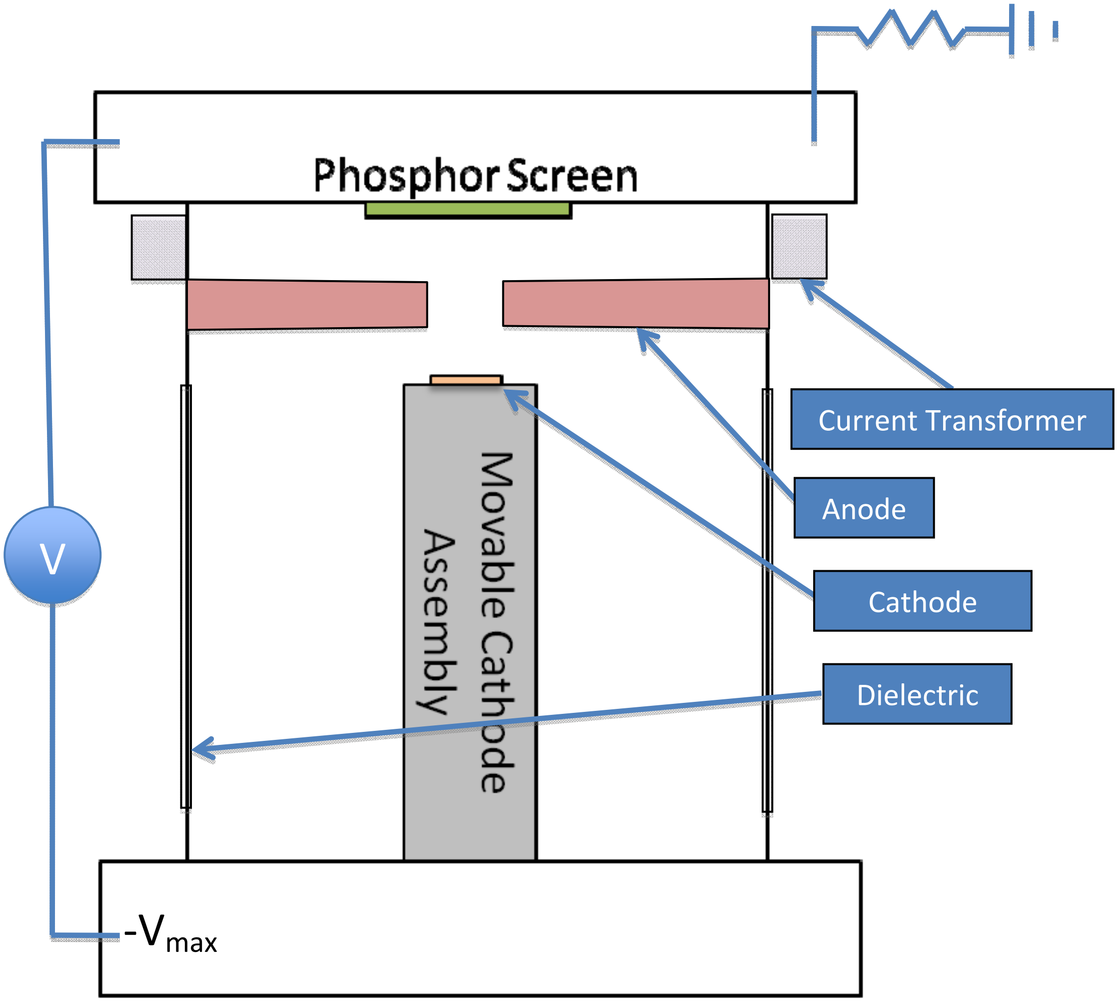

Figure 16. Electrostatic Cathode Test Cell Schematic

C. DESIGN TRADEOFFS AND PARAMETER SELECTION

Experimentally, the emission predicted by Equation {5.1} is generally observable only once the applied field *E* has been raised to some minimum threshold value, dependent on the geometry and material. For the purposes of this thesis, the threshold field is considered to be 10MV/m, and the maximum operating field is 20MV/m. These numbers are roughly characteristic of the DFEA cathodes to be studied at NPS.

In addition to the insulating ceramic pictured above, NPS has on hand a fixed-voltage 100kV power supply suitable for use with this test stand. Field strength adjustment will therefore be made through adjustment of the anode-cathode gap. The pertinent tradeoff is between field strength and gap size: operating with a reduced the gap will achieve higher field but risk causing vacuum arcs, potentially damaging the test cell and cathode.

This tradeoff also affects the placement of the phosphor screen. The simplest arrangement would be to fix the screen directly to the anode, but this creates significant risk of ion blowback as it is bombarded: ions excited off the screen would be positive and therefore be accelerated toward the cathode. This risk can be reduced by placing the screen past the anode in an approximately field-free region; any ions liberated from the screen will remain in its vicinity due to the lack of field instead of accelerating back to damage the cathode. This arrangement, however, requires an aperture in the anode, which will alter the field distribution and potentially defocus the beam. Some setups (including that in Figure 13) mitigate this by spanning the aperture with a grid or "pepperpot," which mostly allows the electrons to pass, but keeps the field roughly uniform. This increases the risk of damaging the cathode and anode, however, albeit less so than with the direct-impingement arrangement. The grid's focusing effects can also lead to emittance degradation. For this design, the aperture will remain ungridded; avoiding arcing and ion blowback is assumed to outweigh the effects of defocusing. This tradeoff remains a viable field of study for future design work.

Though the electron beam will emerge from the cathode approximately collimated and perpendicular to the cathode surface, space-charge forces will tend to defocus the beam as it propagates. Techniques exist to counteract this, including the famous "Pierce geometry" [10]. In a Pierce configuration, the metal surface on which the cathode rests is angled in the direction of beam travel, forcing the local field lines to point inward and help focus the beam. This is shown in Figure 17, where purple lines represent equipotentials and red arrows are local field vectors. The Pierce effect can help mitigate space-charge effects, but since it inherently enhances the field in certain regions, it increases the risk of breakdown. Pierce geometries also reduce the field at the cathode surface however (as is apparent in Figure 17), requiring a smaller gap for the same voltage. In this design, Pierce geometry is included at the cathode support but not analyzed in detail. The topic remains open for optimization in future studies.

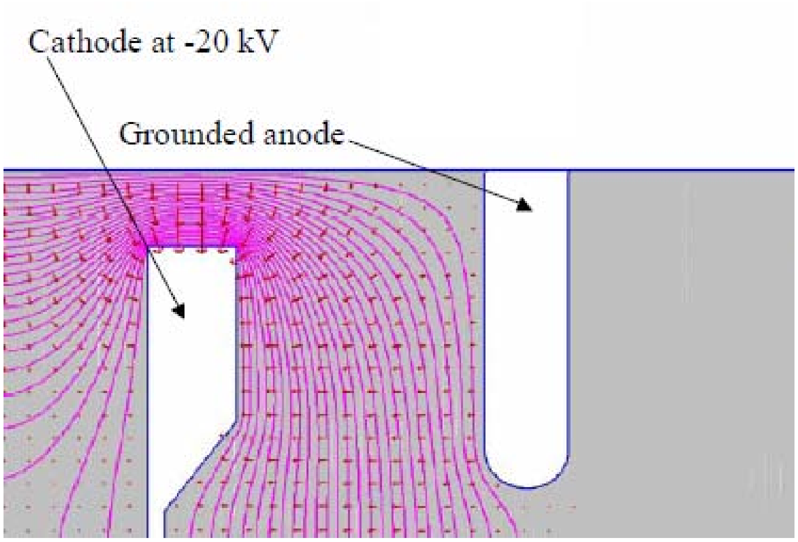

Figure 17. An Example of Pierce Geometry [After 11]

The design's major parameters are summarized in Table 4. The voltage value is fixed by available equipment, and the field strengths represent design goals; the range of gap values is the subject of study below, with initial estimates based on Equation {5.3}.

Parameter	***Value***
Operating Voltage	100kV
Anode-Cathode Gap	5-2.5mm
Operating Field	10-20MV/m

Table 4. Guiding Design Parameters

D. THE DESIGN TOOL: *POISSON SUPERFISH*

First developed at Los Alamos National Laboratory in the late 1970s, *Poisson Superfish* is a suite of programs used to calculate fields (electrostatic, magnetostatic or RF electromagnetic) in two-dimensional geometries. The component programs used for this design work include *Automesh*, which generates a triangular mesh (of variable spacing) fitted to the boundaries of the different regions of the geometry; *Poisson*, which calculates static fields by successive over-relaxation; the *WSFPlot* display tool, used to generate the diagrams shown below; and *SF7*, a postprocessor used to extract specific information from the field map (e.g., field strength along a specified line).

Figure 18 displays an example of *WSFPlot*'s rendering of the region of the schematic indicated. Input geometries are specified in Cartesian coordinates, mapping $x \rightarrow r$ and $y \rightarrow z$ for cylindrically symmetric problems such as this. This is a common approach, and a flag within the input file will cause output tables to be presented as (r,z) instead of (x,y). Output files consist of a table representing the field map. *WSFplot* is used to overlay this on the problem geometry, and includes several useful display options, such as field arrows, equipotential contours and the mesh used.

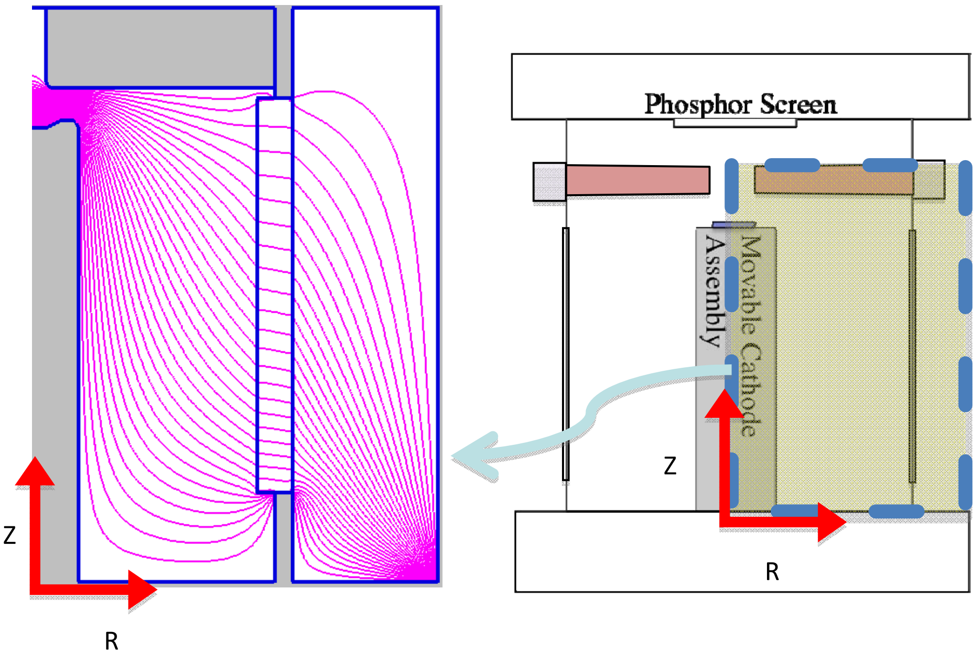

Figure 18. *Superfish* Rendering of Test Cell Interior

The *Superfish* suite is a powerful tool for a wide variety of applications, and includes several additional programs not applicable to this design effort. There are also multiple postprocessors, including tabular display tools. For this thesis, however, all plots were generated in *Matlab* using data from *SF7*.

E. ANODE SHAPE

The baseline concept for an anode in this design is a simple ring. A torus of metal with rectangular cross-section would be easily manufactured and serve the essential purposes of an anode. Figure 19 shows an initial design concept using this type of anode as a close-up of the anode-cathode region. It is a portion of a cross-sectional drawing such as displayed in Figure 18 above; the left border is the test cell's centerline. The red arrows depict the magnitude and direction of the field at given points, while the pink lines are equipotential contours.

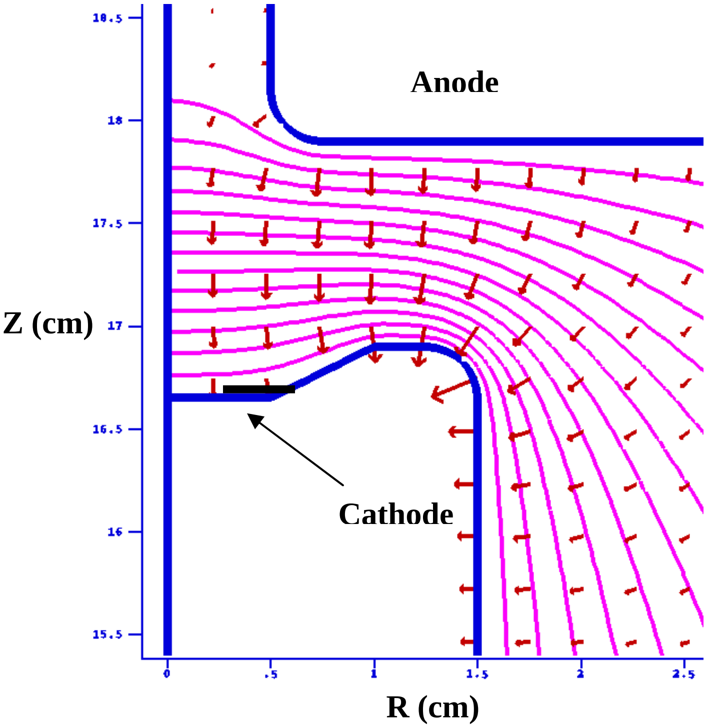

Figure 19. Simple Ring Anode

The anode pictured is rectangular in cross-section, with its lower corner is filleted to avoid creating a field enhancement. This principle is also applied to the outer edge of the cathode support stalk. As the field map shows, the field is elevated in that region even with the fillet; peak field value there should be monitored in future design iterations.

The cathode is pictured in black, resting inside a divot in order to have Pierce focusing. The divot's corners are not filleted, but do not appear to greatly perturb the field distribution. As expected, the field begins to defocus near the anode aperture, as evidenced by the sloping equipotentials.

Figure 20 shows the second general design configuration considered, featuring an angled anode. Angling the lower surface should help alleviate the field concentration near the corner of the cathode support stalk. Angling the top surface helps mitigate damage to the anode by progressively increasing the distance between it and the electron beam. If the anode's angle is greater than that of the diverging electron beam, no electrons will strike (and damage) the anode. Both of these features will affect field distribution; it is pertinent to ask whether they measurably affect field strength at the cathode.

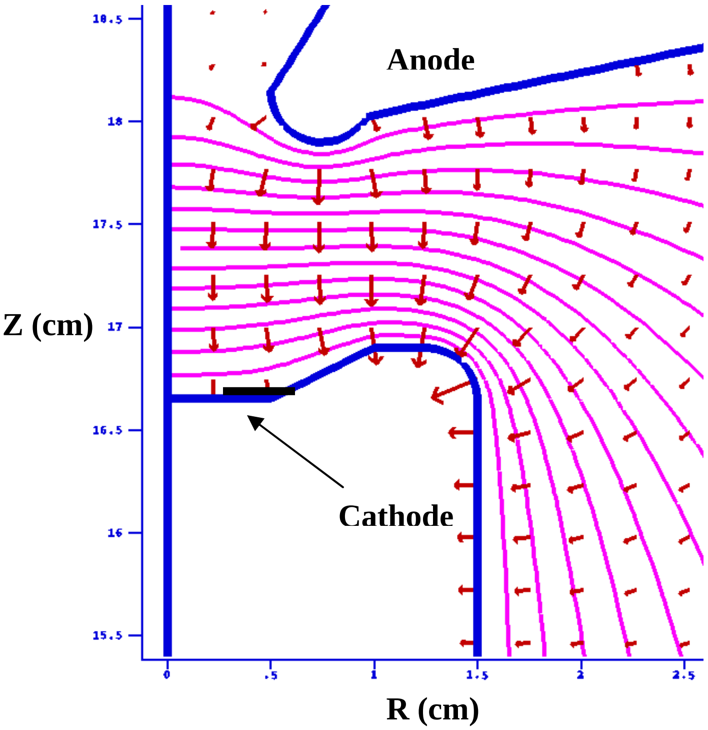

Figure 20. Angled Anode

F. GAP AND APERTURE SPACING

Given a fixed voltage for the power supply, we studied two ways of altering the field distribution at the cathode: anode-cathode gap and anode aperture. The cathode's own geometry has an effect as well, but was not studied as a part of this work. As a baseline, the initial configuration considered for each anode shape uses a 1cm gap, as measured from the top of the cathode support stalk to the lowest point on the anode, and a 1cm aperture. With a potential difference of 100kV, this gap value corresponds to a 10MV/m gradient for infinite parallel plates (see Equation {5.3}). For the actual geometry, the results are significantly lower, as shown in Figure 21, due to Pierce effects and the anode aperture. Field magnitude values are shown as a function of radius out to 5mm, the radius of the cathode divot. The cathode itself will have a radius of approximately 4mm. This baseline configuration data exhibits not only a failure to reach the minimum operating field but also a strong radial dependence in field strength. The fields are reasonably uniform only for the first 1–2mm, corresponding to 25% of cathode area. At a radius of 2mm, the axial field is reduced by 2.5% from its centerline value for both anode shapes.

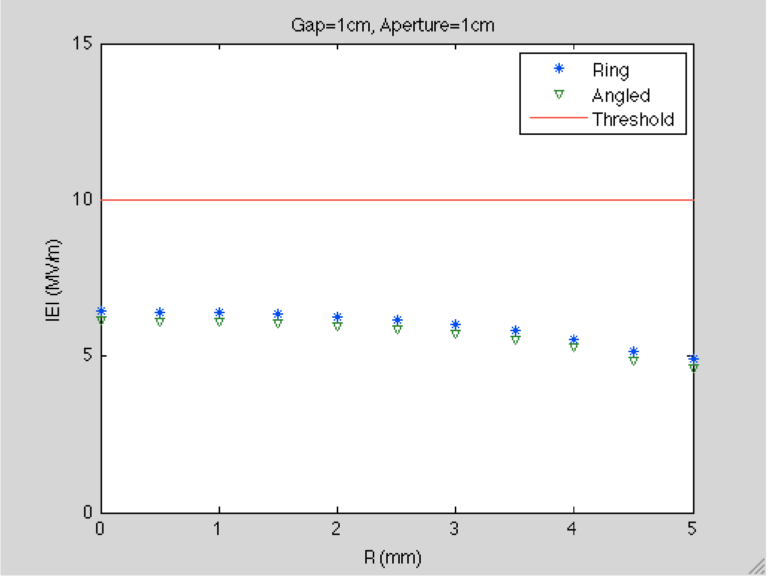

Figure 21. Baseline Design

The next case examined keeps the same gap value but narrows the aperture by half. If this showed improvement in field values, it could present significant advantages, chiefly by flattening out the field in the aperture. As Figure 22 shows, however, the improvement is slight, showing a peak field of 6.6MV/m vs. 6.4MV/m, and the strong radial dependence remains. As before, the simple ring anode provides somewhat more favorable fields, but in this case the disparity is a bit greater. Neither design appears overly promising, and the narrowed aperture introduces the same risks as a pepperpot design. A narrow aperture can even block a portion of the beam. While this is sometimes used in injectors to reduce beam emittance, it is not useful for measuring the cathode's characteristics, and could damage the anode.

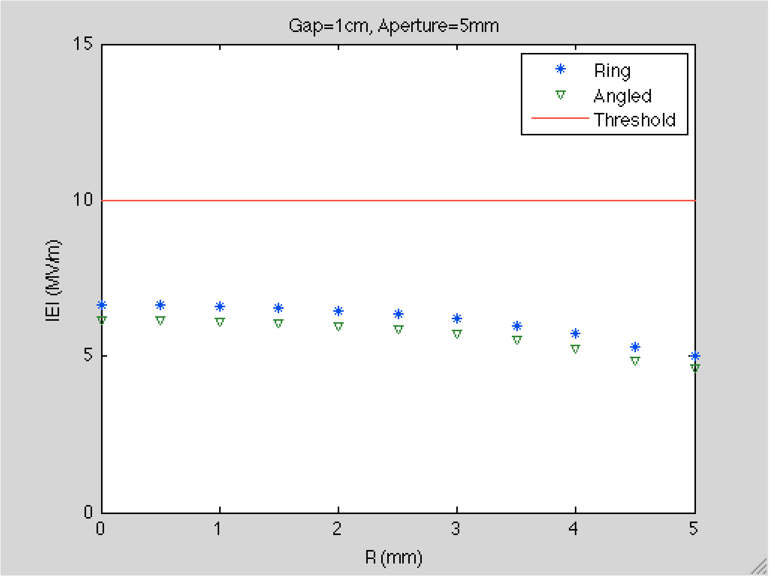

Figure 22. Narrow-aperture Design

The next design iteration returns to the 1cm aperture and halves the gap. The results, seen in Figure 23, show significant improvement. The peak field in this case actually exceeds the target value of 10MV/m. The radial dependence of the field is somewhat lower but still significant, reaching the 2.5% reduction level around 2.5mm. The disparity between the two anode shapes has also narrowed, indicating that the angled anode may be a viable option at this gap spacing. While this case meets the minimum requirements, it is worth investigating yet smaller gap sizes.

Decreasing the gap to 2.5mm produces the results shown in Figure 24. For this case, peak fields fall well within the operating range, and the angled anode performs almost as well as the simple ring. That result is favorable since such a narrow gap carries

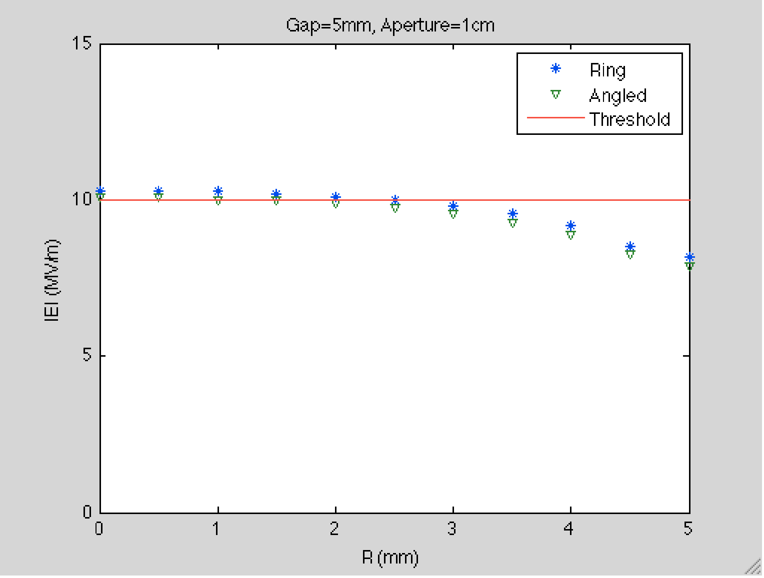

Figure 23. Intermediate-gap Design

increased risk of arcing and the angled anode may be vital to lowering fields outside the cathode region. Even more important a result is the field's uniformity. The field strength only begins to drop off after about 3.5mm, meaning the field is uniform within 2.5% over 75% of the cathode's area.

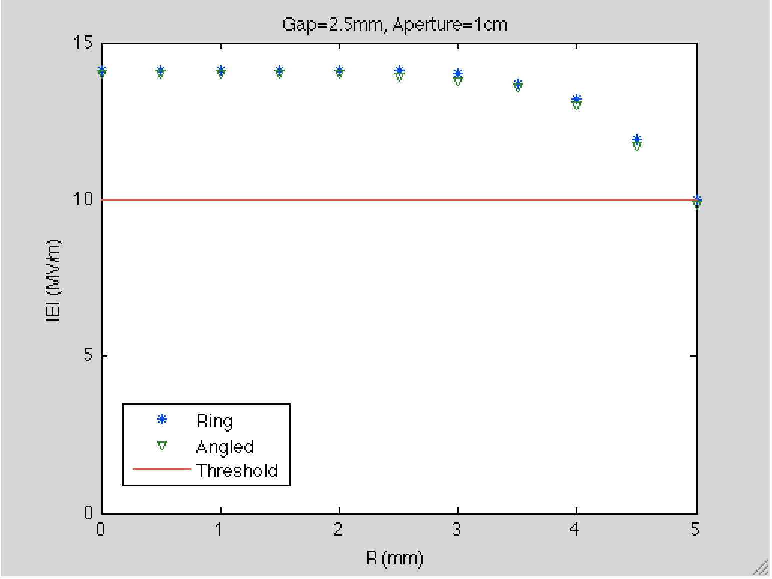

Figure 24. Narrow-gap Design

G. RECOMMENDATIONS

The conflat-cylinder insulator appears entirely feasible for testing cathodes. From a field-strength perspective, a 5mm gap is recommended as the maximum operating setting, and 2.5mm as the nominal setting, using a 1cm or wider aperture. Future design work should examine the possibility of breakdown in the gap and whether an angled anode – perfectly suitable for achieving the required fields at the cathode—would provide mitigation.

LIST OF REFERENCES

[1] Wikipedia Commons: Undulator.png. http://upload.wikimedia.org/wikipedia/commons/9/9f/Undulator.png (accessed 19 Oct 2009).

[2] S. Sasaki, "Analyses for a Planar Variably-Polarizing Undulator." *Nuclear Instruments and Methods in Physics Research* A347, pp. 83–86, 1994.

[3] S.H. Kim, "Achievable Magnetic Fields in Super-Ferric Helical Undulators for the ILC." ANL/APS/LS-311, Argonne National Laboratory, 13 April 2006.

[4] W.B. Colson, C. Pellegrini, and A. Renieri, Eds., *Free Electron Laser Handbook*. The Netherlands: Elsevier Science Publishing Co. Inc., 1990.

[5] J. Blau, "Multimode Simulations of Free-Electron Lasers." PhD. dissertation, Naval Postgraduate School, Monterey, CA, 2002.

[6] W.M. Fawley. *User Manual for GINGER and its Postprocessor XPLOTGIN* v. 1.3f. Report LBNL-4925. Livermore, CA: Lawrence Berkeley National Laboratory, 2001

[7] J.D. Jarvis, *et al.*, "Transverse Emittance of Diamond Field-Emitter Arrays." *Proceedings of the 30th Annual Free-Electron Laser Conference*. Gyeongju, Korea, 2008.

[8] S.T. Pai and Q. Zhang. *Introduction to High Power Pulse Technology*. Hackensack, NJ: World Scientific, 1995.

[9] J.D. Jarvis, *et al*, "Uniformity Conditioning of Diamond Field-Emitter Arrays." *Proceedings of the 30th Annual Free-Electron Laser Conference*. Gyeongju, Korea, 2008.

[10] J.R. Pierce, *Theory and Design of Electron Beams.* New York: Van Nostrand, Co., 1949.

[11] N. Vinogradov, *et al*, "Polarized Pulsed Beam Source for Electronic Microscopy." *Proceedings of the 21st Annual Particle Accelerator Conference,* Albuquerque, 2007.

THIS PAGE INTENTIONALLY LEFT BLANK

INITIAL DISTRIBUTION LIST

1. Defense Technical Information Center
Ft. Belvoir, Virginia

2. Dudley Knox Library
Naval Postgraduate School
Monterey, California

3. Chairman, Department of Physics
Naval Postgraduate School
Monterey, California

4. Prof. William B. Colson
Naval Postgraduate School
Monterey, California

5. William Fawley
Lawrence Berkeley National Laboratory
Berkeley, California

6. Quentin Saulter
Office of Naval Research
Arlington, Virginia

7. Michael Deitchman
Office of Naval Research
Arlington, Virginia